Science Advances
MAAAS

Supplementary Materials for

On-skin paintable biogel for long-term high-fidelity electroencephalogram recording

Chunya Wang, Haoyang Wang, Binghao Wang, Hiroo Miyata, Yan Wang,
Md Osman Goni Nayeem, Jae Joon Kim, Sunghoon Lee, Tomoyuki Yokota,
Hiroshi Onodera, Takao Someya*

*Corresponding author. Email: someya@ee.t.u-tokyo.ac.jp

The PDF file includes:

Supplementary Text
Figs. S1 to S32
Tables S1 and S2
Legend for movie S1
References

Other Supplementary Material for this manuscript includes the following:

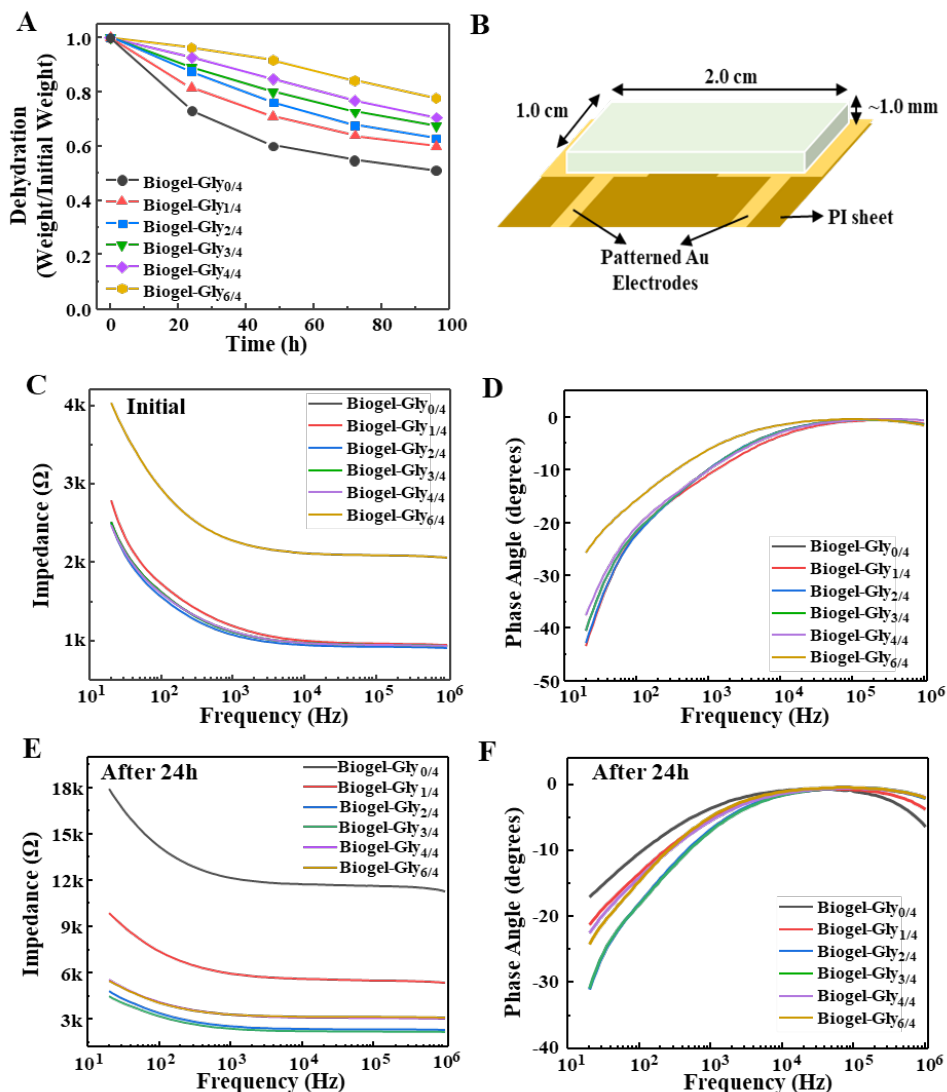Movie S1

Supplementary Text

Fig. S1. Influence of glycerol content on dehydration and electrical impedance properties of biogels. (A) Dehydration properties of biogels with different glycerol contents. (B) Schematic illustration of the electrical impedance measuring setup. (C, D) Initial electrical impedance spectroscopy test results of biogels with different glycerol contents. (E, F) Electrical impedance spectroscopy test results of such biogels after 24 h.

The recipes for biogels with different glycerol contents are listed in Table S1. To measure the electrical impedance of the biogels with different glycerol contents, biogels with a rectangular shape and thickness of ~1.0 mm were painted on two patterned Au electrodes on a polyimide (PI) sheet (Fig. S1B), and an LCR meter (E4980AL, KEISIGHT) was connected to the Au electrodes to record the impedance.
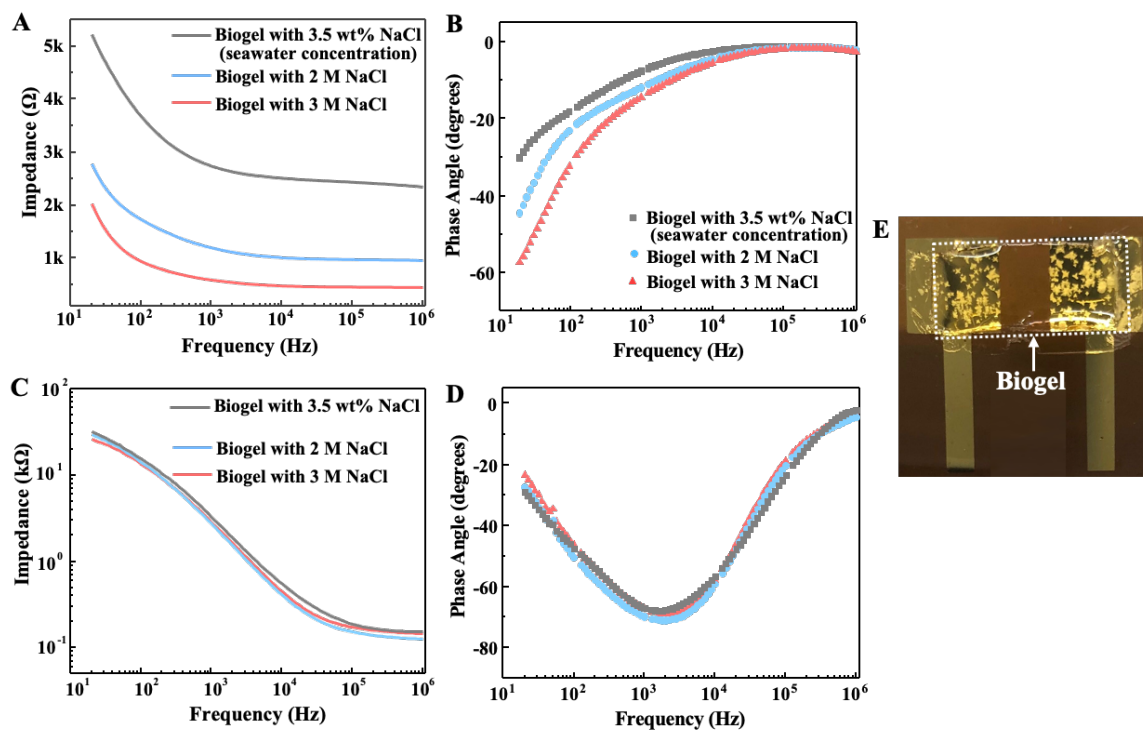
Fig. S2. Influence of NaCl content on electrical impedance of biogels. (A, B) Electrical impedance spectroscopy test results of biogels with different NaCl contents. (C, D) Skin contact impedance spectroscopy test results with biogels containing different NaCl contents as interfaces. (E) Photo of painted biogel with 3 M NaCl after being kept for 48h, showing some crystallization of NaCl in the biogel matrix. All of the concentration of NaCl was calculated based on deionized water volume.

The intrinsic impedances of biogels with different NaCl contents were measured using the same measuring setup shown in Fig. S1B. The recipes for the biogels with different NaCl contents are listed in Table S1. Although the biogel with a higher NaCl content showed higher ionic conductivity (lower intrinsic impedance, Fig. S2A), some NaCl dissolved out from the biogels with higher NaCl content after being kept for 48 h, which is consistent with the previous observation (*39*).
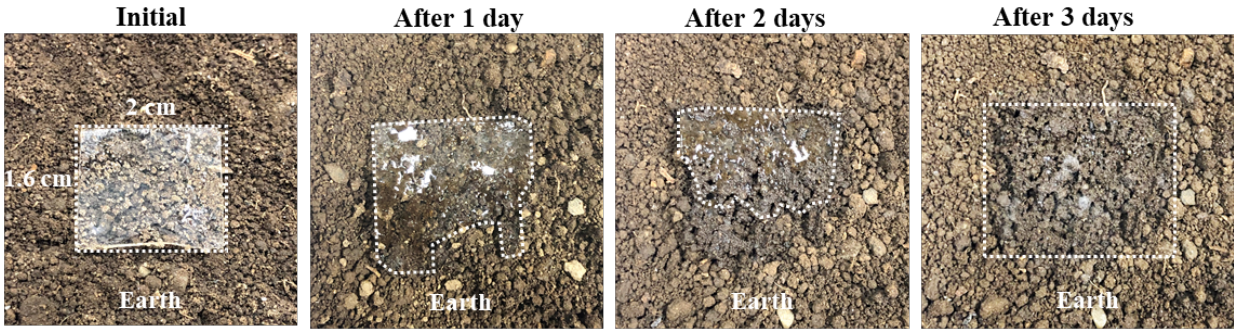
Fig. S3. Biodegradability of biogel. Photographs of the biodegraded biogel film in the soil after different days.

To investigate the biodegradability of the as-developed gelatin-based biogel, a simulated biodegradation experiment was conducted by placing a pre-formed biogel film on soil. The morphological changes of the biogel were checked by the naked eye and were captured by a camera every day. As shown in Fig. S3, the biogel film began to degrade on the soil on the first day and the soil was completely degraded after 3 days, because of the microbial corrosion of the gelatin (*40*).

Fig. S4. **Inferior mechanical interaction of commercial EEG gel with electrodes.** Photographs of detached stiff and flexible Ag/AgCl electrodes from the commercial EEG adhesive gel on the skin when pulling these electrodes.
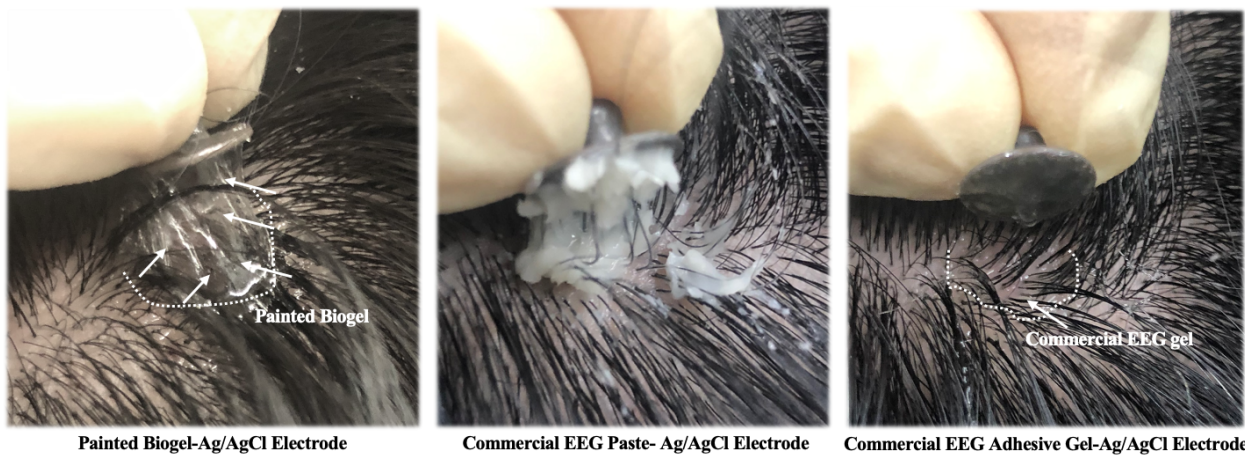

Fig. S5. Superior mechanical interaction of painted biogel with hairy scalp to commercial EEG paste/gel. Photographs showing Ag/AgCl electrode state when pulling these electrodes from the painted biogel, commercial EEG paste and commercial EEG adhesive gel on the hairy scalp.
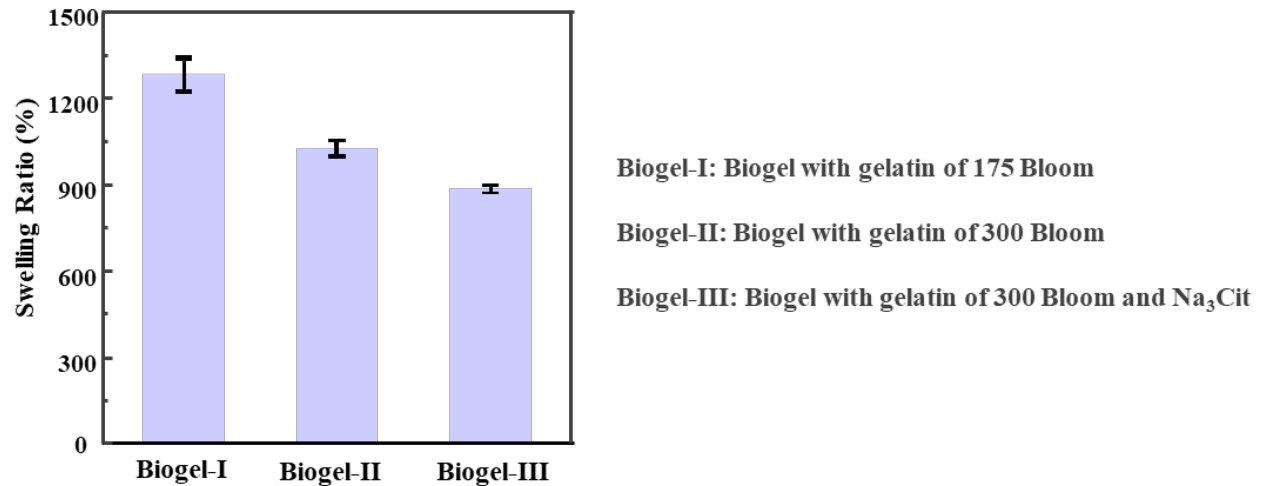
Fig. S6. Swelling properties of biogels. Swelling ratio of biogels based on 175 Bloom gelatin, 300 Bloom gelatin and 300 Bloom gelatin with Na3Cit after swelling in DI water for 48 h.

To analyze the relative degrees of cross-linking in the biogel, swelling experiments were performed to determine the biogel swelling ratio as calculated by dividing the weights of the fully swollen biogels by the weights of dry biogels. A decreased swelling ratio indicates increased levels of cross-linking in the gel matrix (*41*). The biogels were pre-swollen by immersing them in DI water at room temperature for 48 h. The fully swollen samples were weighed after the excess surface water was removed with a filter paper. The swollen biogels were then kept in a vacuum chamber for 48 h to achieve fully dry samples, and the weights of the dry samples were measured.
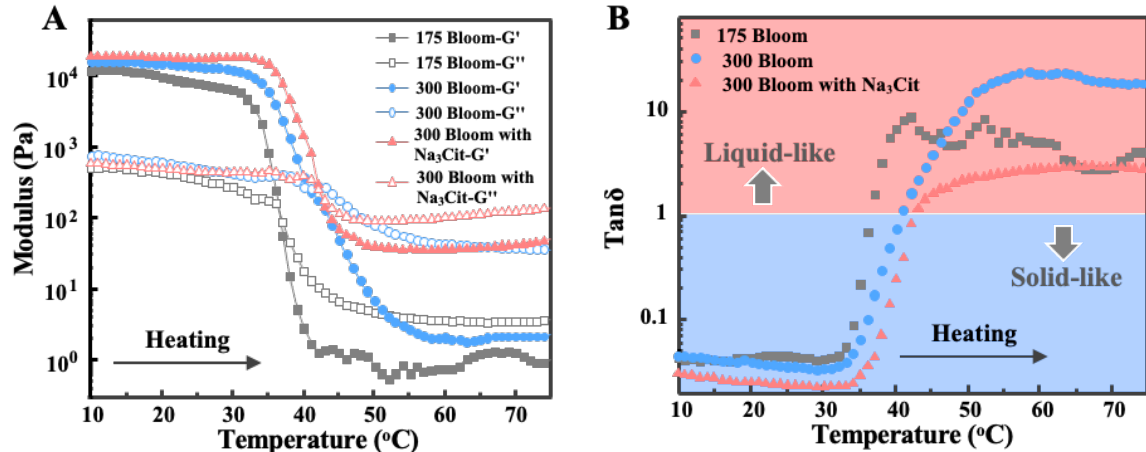
Fig. S7. Rheological property of biogels. (A) Rheological characterization of biogels based on 175 g Bloom gelatin, 300 g Bloom gelatin and 300 g Bloom gelatin with Na_3Cit at a temperature sweep from 10 to 75 °C, showing their transition between elastic gel state and viscous liquid state. (B) The corresponding tanδ (G''/G') calculated from the data in (A).

To verify their transition from a solid-like gel state to a viscous liquid state, the rheological properties of the biogels (Biogel-175 g Bloom, Biogel-300 g Bloom and Biogel-300 g Bloom with Na_3Cit formulation) in response to temperature changes during the heating process were characterized (Fig. S7A and S7B). During the heating process, both the storage modulus G' and loss modulus G'' for all of the biogels decreased continuously with increasing temperature (Fig. S7A), and the corresponding tanδ (G''/G') increased beyond one at above 45 °C for the biogels (Fig. S7B), indicating their transition from viscoelastic gel to viscous liquid at high temperature. The high transition temperature of the optimized biogel from solid-like viscoelastic gel to viscous fluid would make it possible for this biogel to work at the regions of normally hot weather.
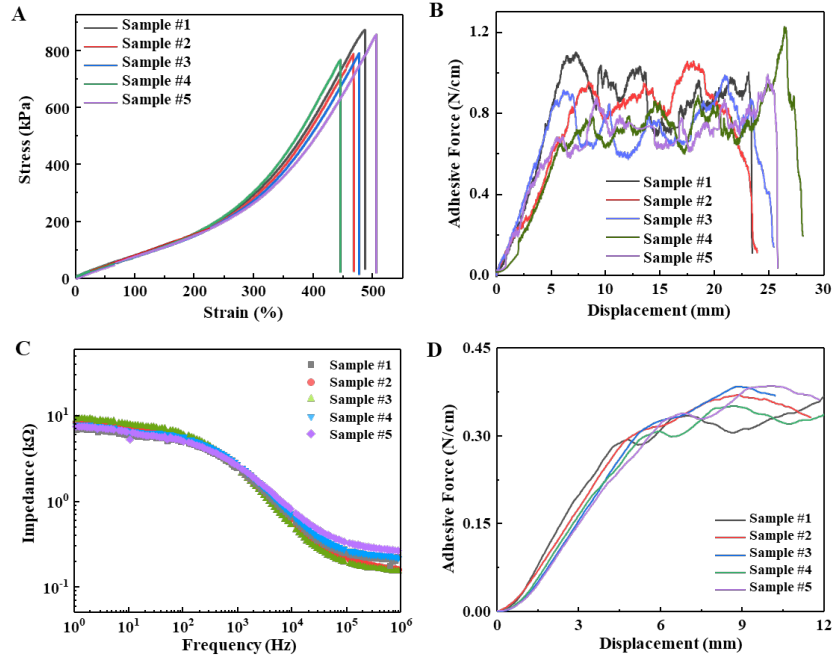
Fig. S8. Mechanical, electrical, and adhesive characteristics for biogels. (A) Stress–strain curves of five biogel samples at ambient temperature. (B) Biogel-skin interfacial adhesion force for five on-skin painted biogels. (C) Electrode-hairy scalp impedance spectra for five on-skin painted biogel samples. (D) Biogel-electrode interfacial adhesion force for five on-skin painted biogel samples.
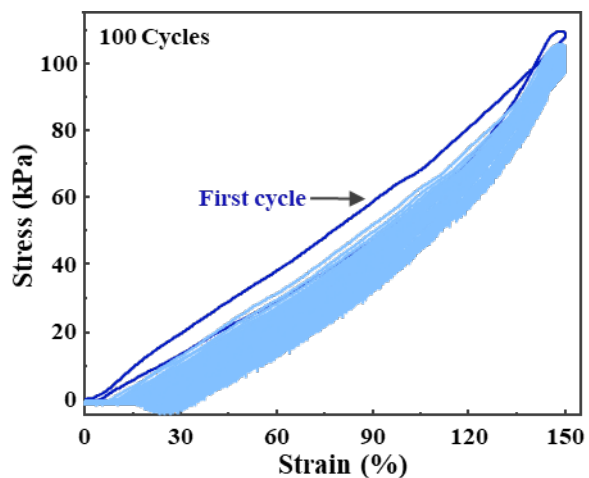
Fig. S9. Mechanical durability of biogel. Cyclic tensile loading–unloading curves of the optimized biogel at ambient temperature, showing its mechanical robustness. The dark blue curve refers to the first tensile loading–unloading cycle.

The biogel exhibited a distinct hysteresis loop in the first tensile loading–unloading cycle, which was contributed to the dissipation of plenty of energy induced by rapid dissociation of the physical interactions in the biogel network, demonstrating the viscoelastic feature of the biogel.
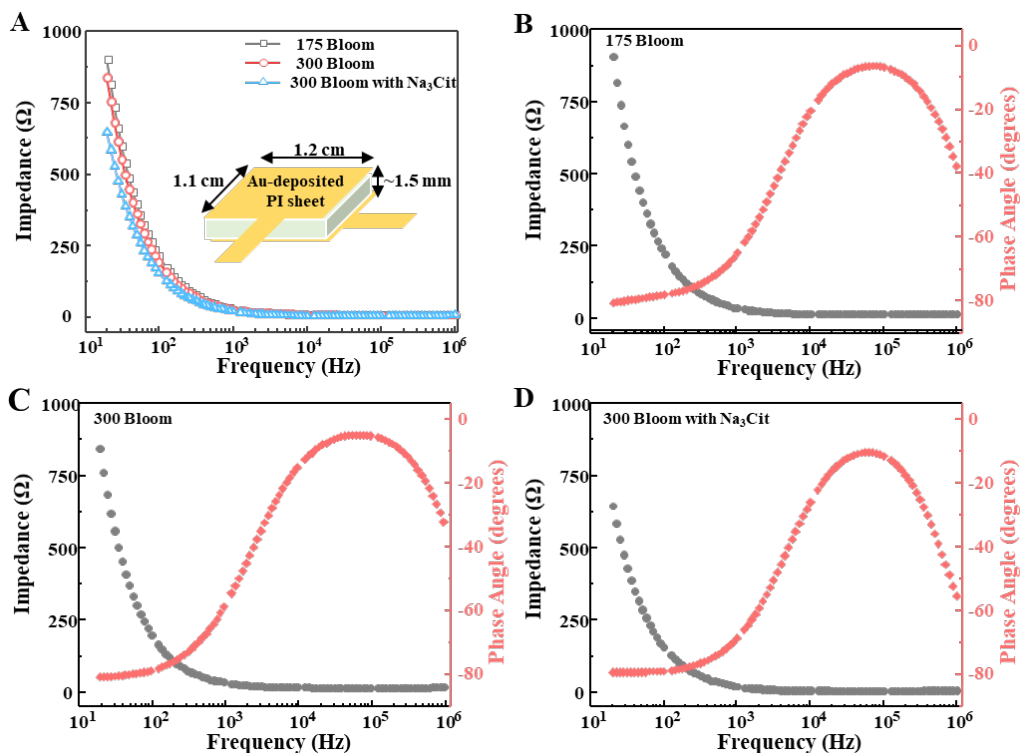
Fig. S10. Electrical impedance of biogels. (A-D) Electrical impedance spectroscopy measurements in the thickness direction of biogels based on 175 g Bloom gelatin, 300 g Bloom gelatin and 300 g Bloom gelatin with Na_3Cit. Inset in (A) shows the impedance measuring setup.

At high frequencies from 10^2–10^5 Hz, the biogels based on 175 g Bloom gelatin, 300 g Bloom gelatin, and 300 g Bloom gelatin with Na_3Cit showed similar low impedances. At the frequencies below 10^2 Hz, the optimized biogel showed a lower impedance, as the introduction of Na_3Cit enhanced the amount of free ions in the biogel matrix.
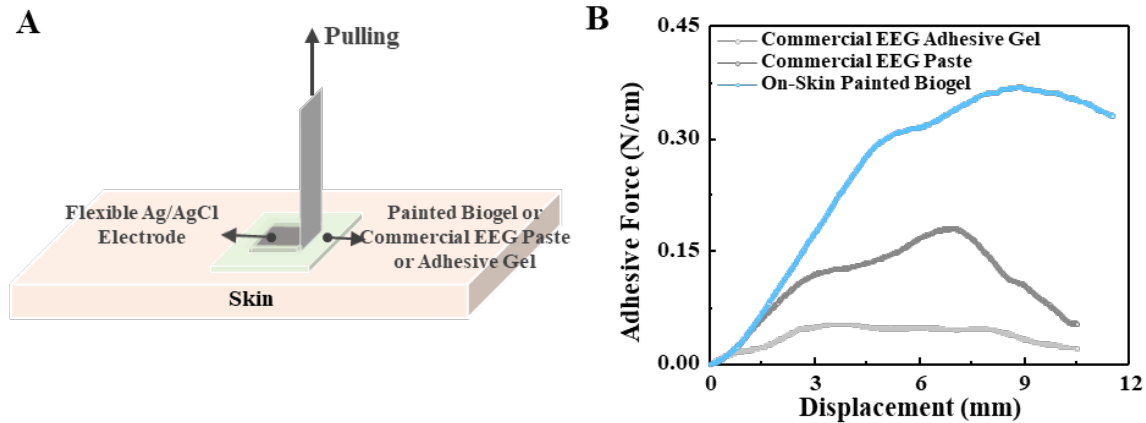
Fig. S11. Interfacial adhesion properties between flexible electrodes and commercial EEG paste/gel, on-skin painted biogel. (A) Schematic illustration showing interfacial adhesiveness test between flexible Ag/AgCl electrode and gels through a 90° peeling process. (B) Interfacial adhesion force of on-skin painted biogel-Ag/AgCl electrode interface, commercial EEG paste-Ag/AgCl electrode interface, and commercial EEG adhesive gel-Ag/AgCl electrode interface.

The gel–electrode interfacial adhesive force was measured using the measurement setup illustrated in Fig. S11A. The biogel, commercial EEG paste, or commercial adhesive liquid gel was painted on the forearm skin, and flexible Ag/AgCl electrodes were placed on the painted biogel/paste/adhesive liquid gel. Then a 90° pulling was applied to the flexible Ag/AgCl while simultaneously measuring the pulling force.
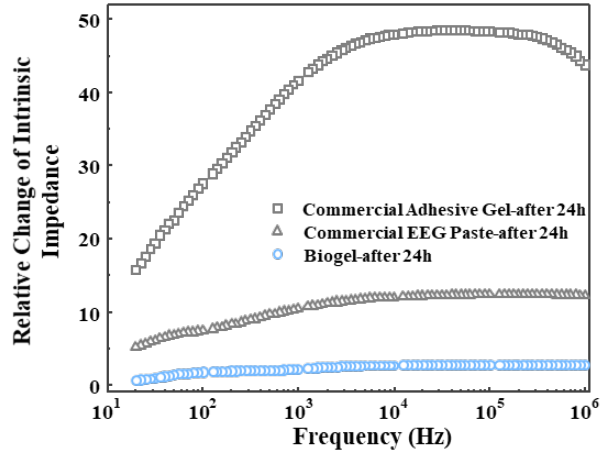
Fig. S12. Superior long-term stability of the as-prepared biogel. Relative change of electrical impedance of painted biogel, commercial EEG paste and commercial adhesive gel after being kept in the room environment for 24 h.

The electrical impedances of the biogel, commercial EEG paste, and adhesive gel were measured according to the setup shown in Fig. S1B. The relative impedance change was calculated based on the initial impedance and impedance after 24 h.
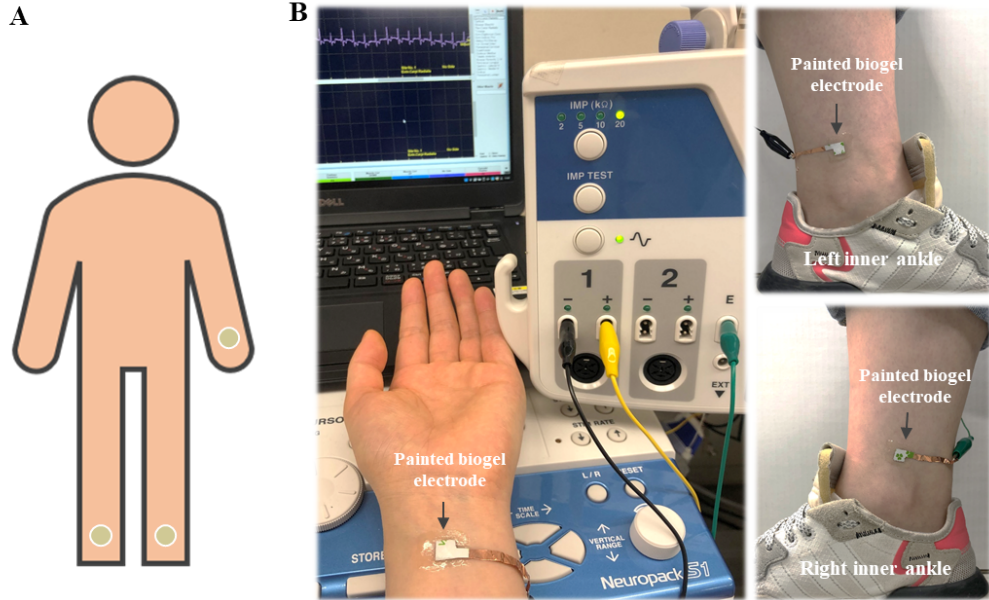
Fig. S13. ECG recording setup. (A) Schematic illustration showing the electrode placement for ECG recording in the sedentary state. (B) Photographs (right) showing the electrode position and experimental setup for ECG recording.

For ECG recording in a sedentary state, three on-skin painted biogel electrodes were placed at the wrist and ankle positions, as shown in Fig. S13A, and then were connected to a signal-recording system (Fig. S13B).
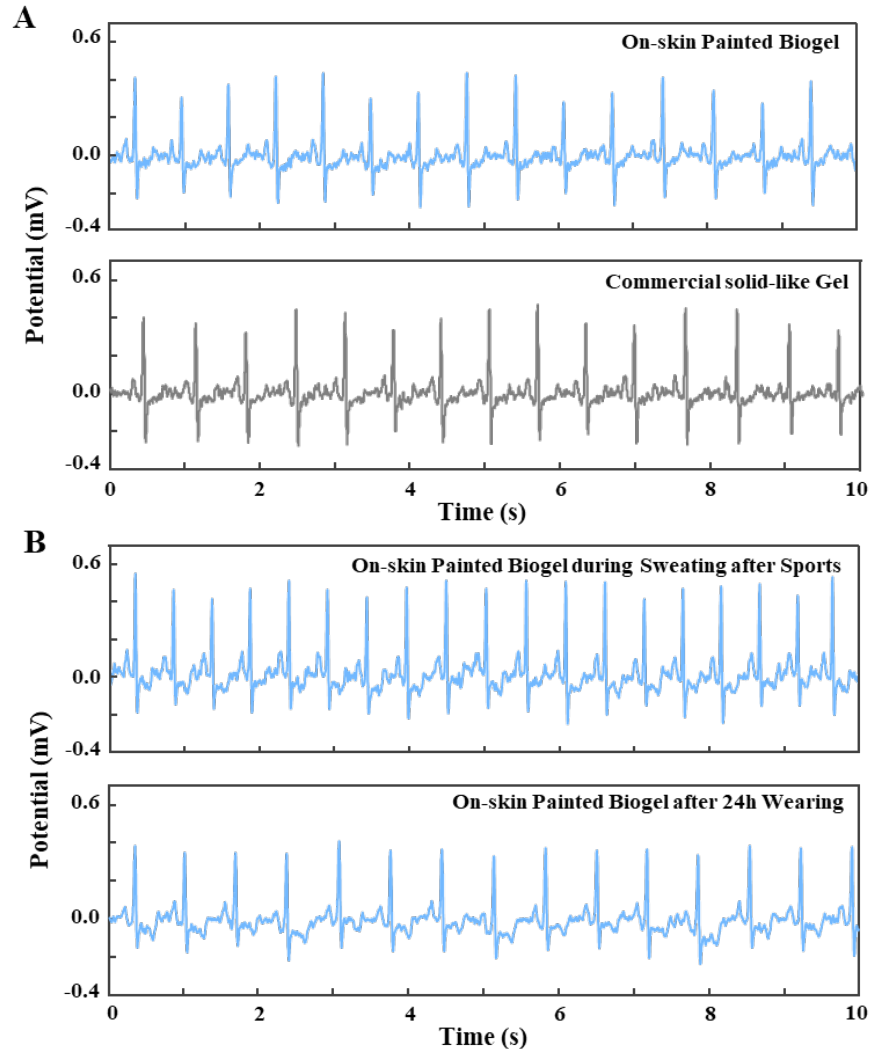
Fig. S14. High-quality ECG recording by on-skin painted biogel electrodes. (A) ECG signals recorded by on-skin painted biogel electrodes (upper) and commercial gel electrodes (lower). (B) ECG signals recorded by on-skin painted biogel electrodes after workout-induced sweating (upper) and after 24 h continuous wearing (lower).
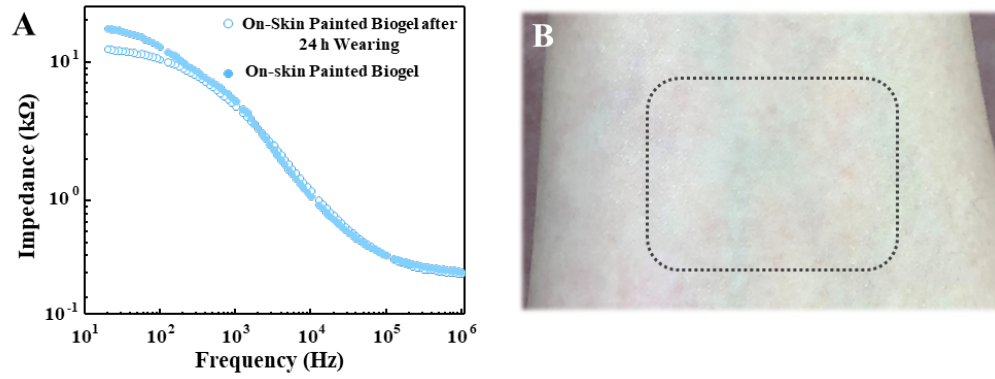
Fig. S15. Skin contact impedance and good biocompatibility of biogel. (A) Electrode–skin impedance spectra for on-skin biogel (initially painted and after 24 h continuous wearing on skin). (B) photos of the skin surface where on-skin painted biogel was mounted and removed after 24 h, showing the biocompatibility of the painted biogel.
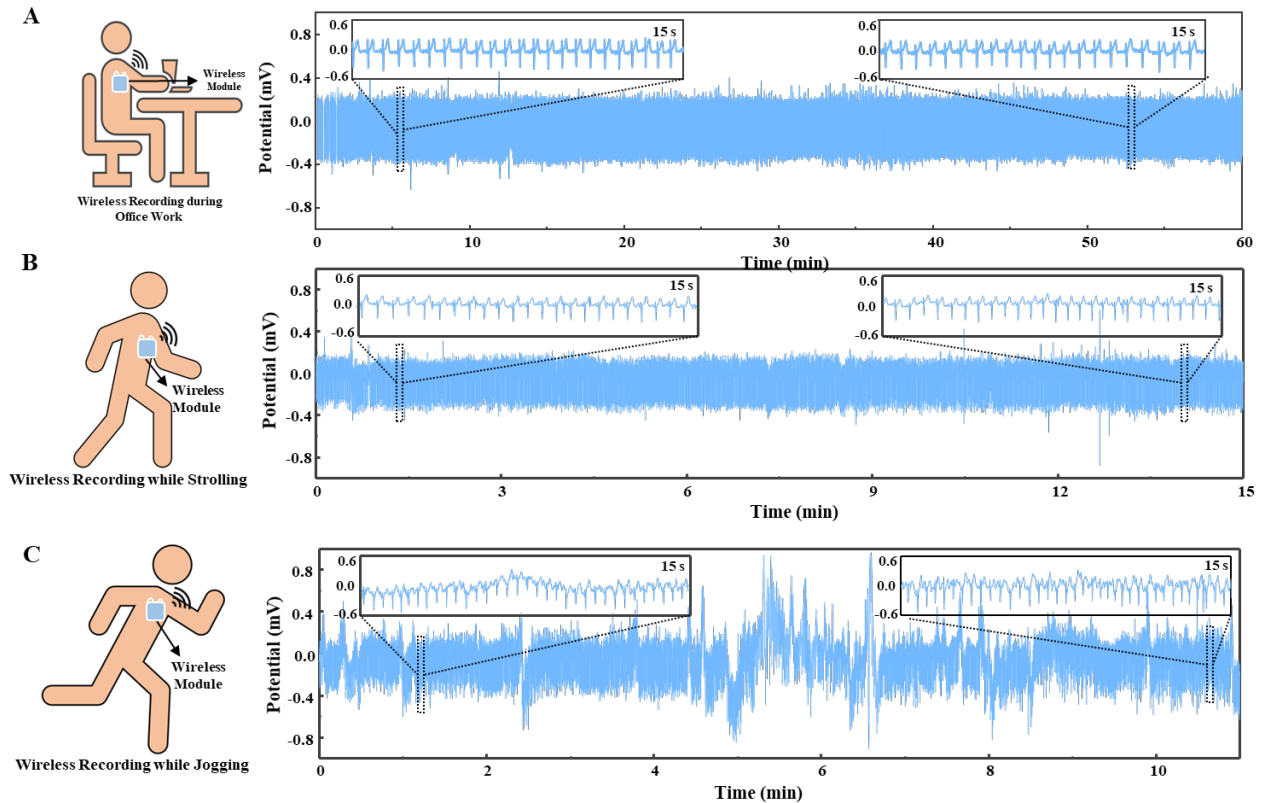
Fig. S16. Wireless ECG recording by on-skin painted biogel electrodes. (A) Schematic illustration showing the wireless recording of ECG during office work (left) and raw ECG signals wirelessly and continuously recorded by painted biogel electrodes during office work (right). (B) Schematic illustration of wireless ECG recording during strolling (left) and raw ECG signals continuously recorded while the subject strolls (right). (c) Schematic illustration of wireless ECG recording during jogging (left) and raw ECG signals continuously recorded while the subject jogs (right).

For the wireless ECG recording, two on-skin painted biogel electrodes were integrated with a commercially available wireless module with recording, processing and transmission circuits to wirelessly monitor the ECG signals during daily activities. Various representative daily activities, including executing office work, walking, and jogging, were performed for a long period (see illustration shown in Fig. S16), and the meanwhile ECG signals were continuously monitored by the painted biogel electrodes with the wireless circuit module. The recorded raw ECG signals during office work, walking, and jogging are plotted in Fig. S16, which shows distinguishable informative sub-waves and long-term stability, indicating the capability of the painted biogel to sufficiently capture ECG signals during normal daily activities.
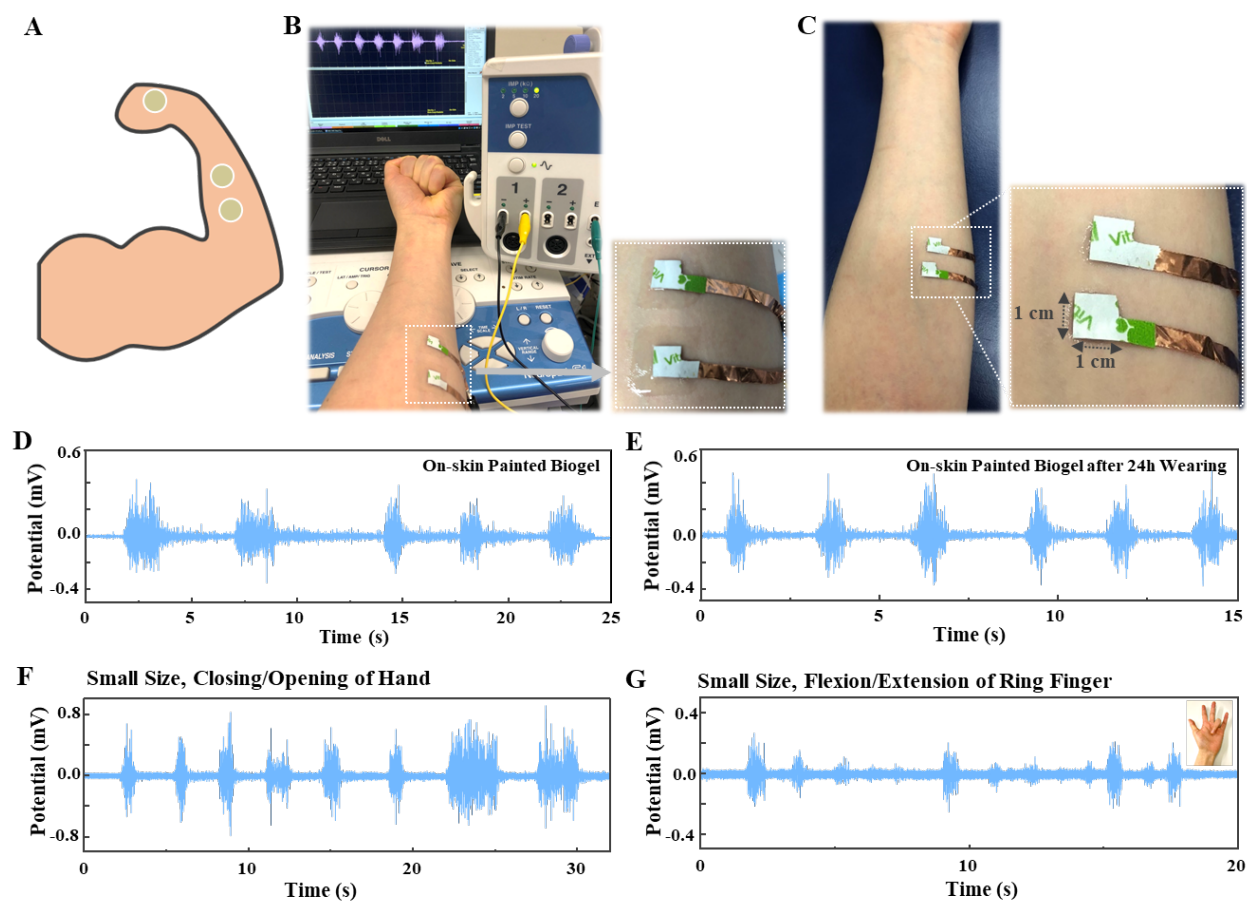
Fig. S17. High-quality EMG recording by on-skin painted biogel electrodes. (A) Schematic illustration showing the electrode placement for EMG recording. (B, C) Photographs showing the experimental setup for recording EMG signals from flexor carpi radialis (B) and the small-sized painted biogel electrodes for EMG recording (C). (D, E) EMG signals recorded by pristine painted biogel electrodes (D) and by biogel electrodes after 24 h continuous wearing (E). (F, G) EMG signals recorded by small-sized painted biogels when the subject closed and opened the hand (F) and when the subject flexed and extended the ring finger (G).

As a proof of concept of the EMG recording by the on-skin painted biogel electrodes, the EMG signals generated by the brachioradialis muscle during hand closing/opening were recorded by three painted biogel electrodes placed on the forearm and hand dorsum position (Fig. S17A) and connected to a signal-recording system (Fig. S17B). Both the freshly painted biogel electrodes and those electrodes after 24 h of continuous wearing could capture clear and high-quality EMG signals, and the overall signals recorded by the biogel electrodes after 24 h of wearing showed no significant differences relative to those monitored by the fresh biogel electrodes (Fig. S17D and 17E). In addition, smaller-sized on-skin painted biogel electrodes (Fig. S17C), could also effectively detect EMG signals. The EMG signals induced by full hand closing/opening (Fig. S17F) and relatively low-amplitude EMG signals produced by the flexion/extension of the ring finger (Fig. S17G) were successfully recorded with high quality by the small-sized painted biogel electrodes. This result is meaningful for the recording weak EMG signals generated by various subtle muscle activities.
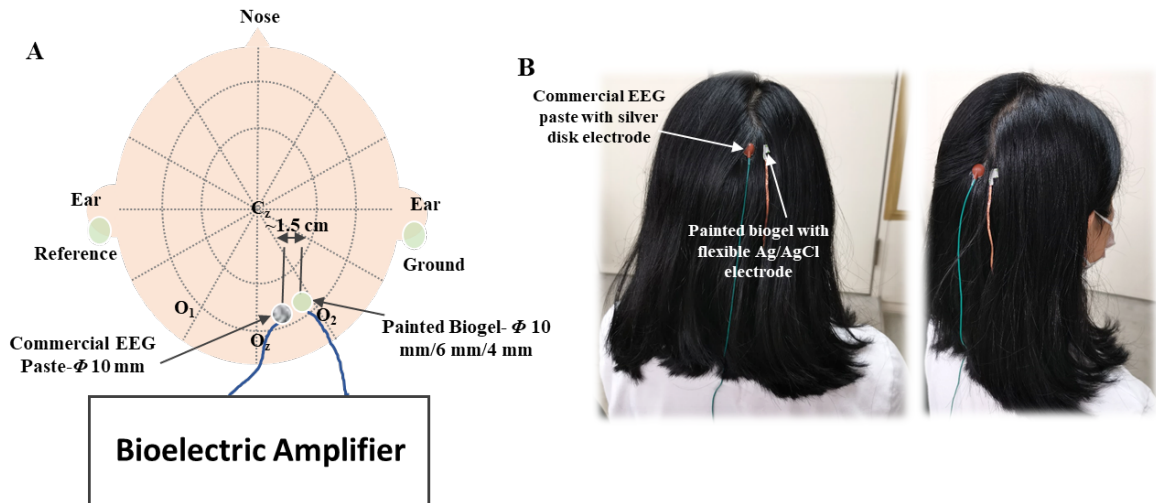
Fig. S18. EEG recording by on-skin painted biogel electrodes. (A) Schematic illustration of the experimental setup for dual-channel EEG recording. (B) Photographs showing the position of the painted biogel electrode and commercial EEG paste electrode on a scalp with dense hairs. The standard silver disk electrode was used for commercial EEG paste, and the flexible Ag/AgCl electrode was used for the painted biogel. These two electrodes were connected to the dual-channel bioelelctric amplifier for EEG recording.
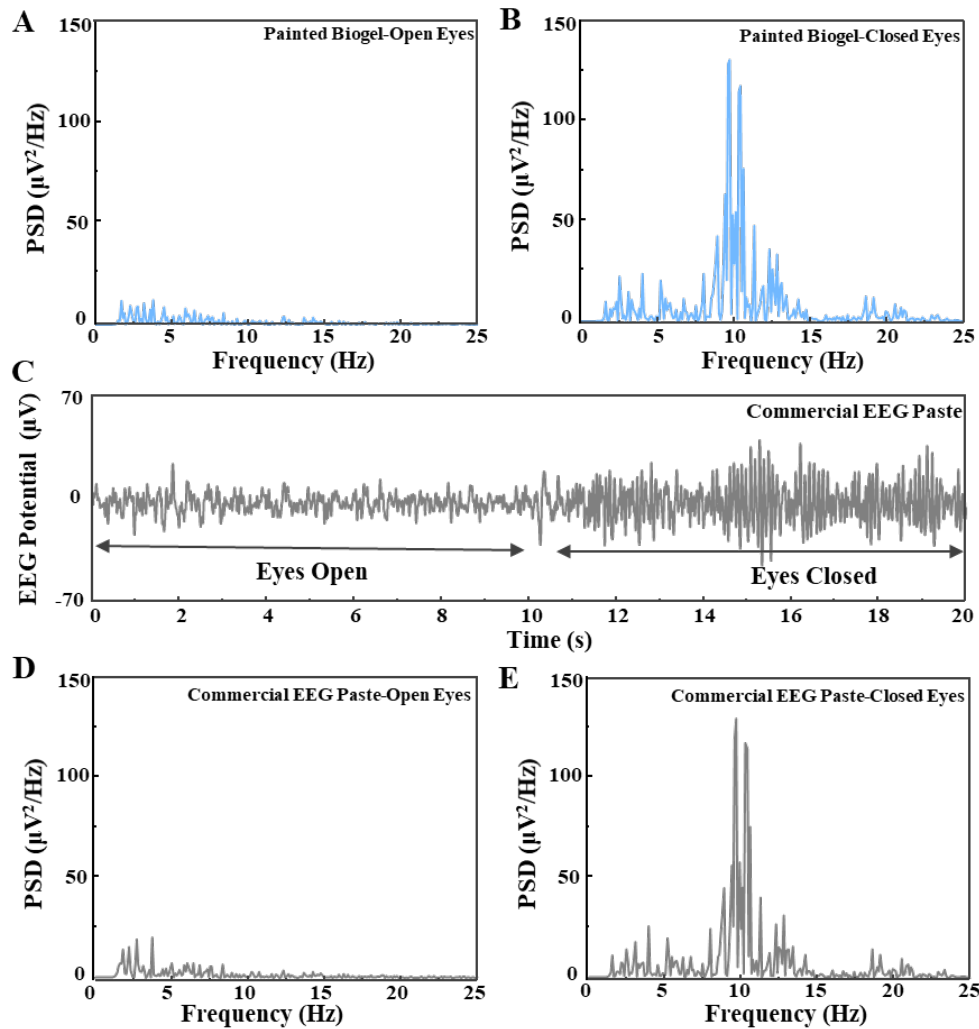
Fig. S19. EEG recording by biogel electrodes and commercial EEG paste electrode in the eyes-open/closed paradigm. (A, B) Power spectral density (PSD) calculated from EEG signals recorded by the painted biogel electrode during open eyes (A) and closed eyes (B), showing clear alpha rhythm features at approximately 10 Hz for EEG signals during closed eyes. (C) EEG signals recorded by the commercial EEG paste electrode in the eyes-open/closed paradigm. (D, E) PSD calculated from EEG signals in (C) during open eyes (D) and closed eyes (E).
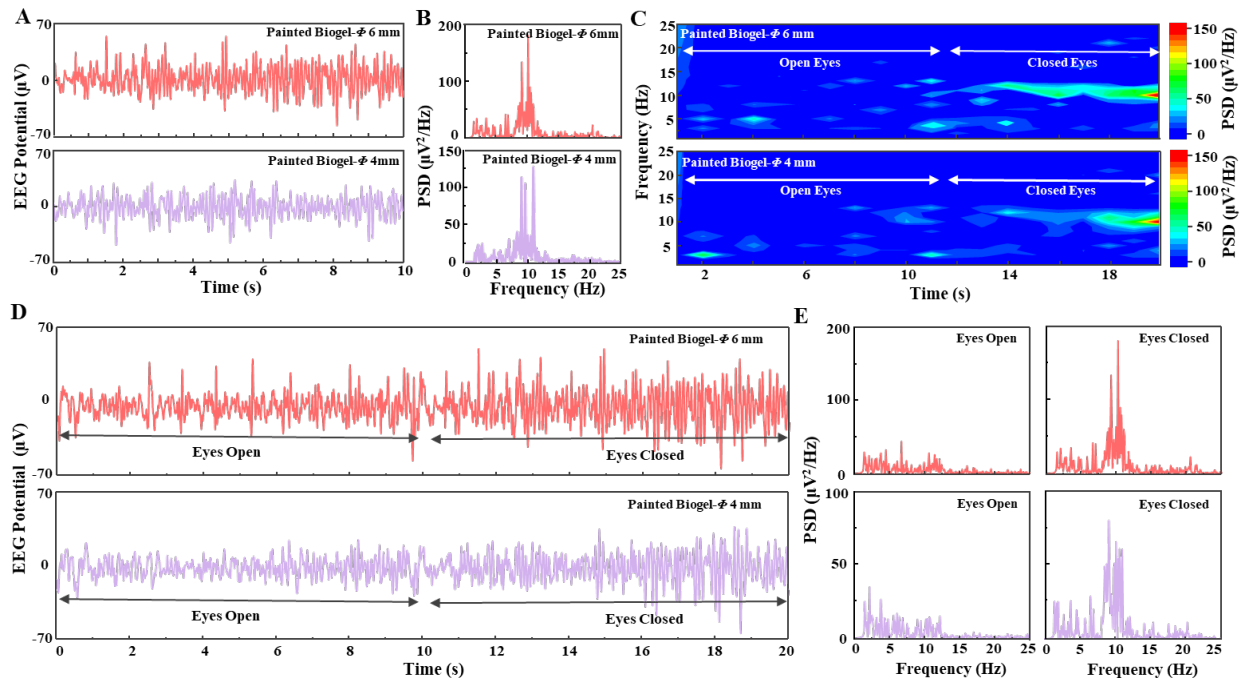
Fig. S20. EEG recording by small-sized on-skin painted biogel electrods. (A) EEG alpha rhythms recorded by the painted biogel electrodes with diameter of ~6 mm (upper) and ~4 mm (lower). (B) PSD calculated from EEG alpha signals in (A). (C) Spectrograms of EEG signals in the eye open/closed paradigm, showing clear alpha rhythms in the eye-closed state. (D) EEG signals recorded by the painted biogel electrodes with diameter of ~6 mm (upper) and ~4 mm (lower) in the eye open/closed paradigm. (E) PSD calculated from eye-open and eye-closed EEG signals in (D).

The electrodes based on small-sized painted biogels with diameters of ~6 mm and ~ 4mm showed high-quality EEG alpha rhythm recordings with a clear characteristic alpha rhythm central peak at 10 Hz (Fig. S20A and 20B). Distinct differences between the EEG signals in the eyes-open and eyes-closed states were also detected by the small-sized painted biogel electrodes, which showed that no alpha rhythm in the eyes-open paradigm, and evident alpha rhythms in the eyes-closed state (Fig. S20C-E).
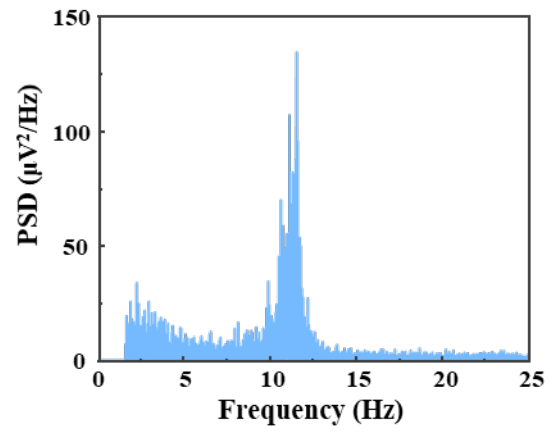
Fig. S21. Overall PSD. The PSD was calculated from the overall continuously recorded EEG alpha rhythm signals.
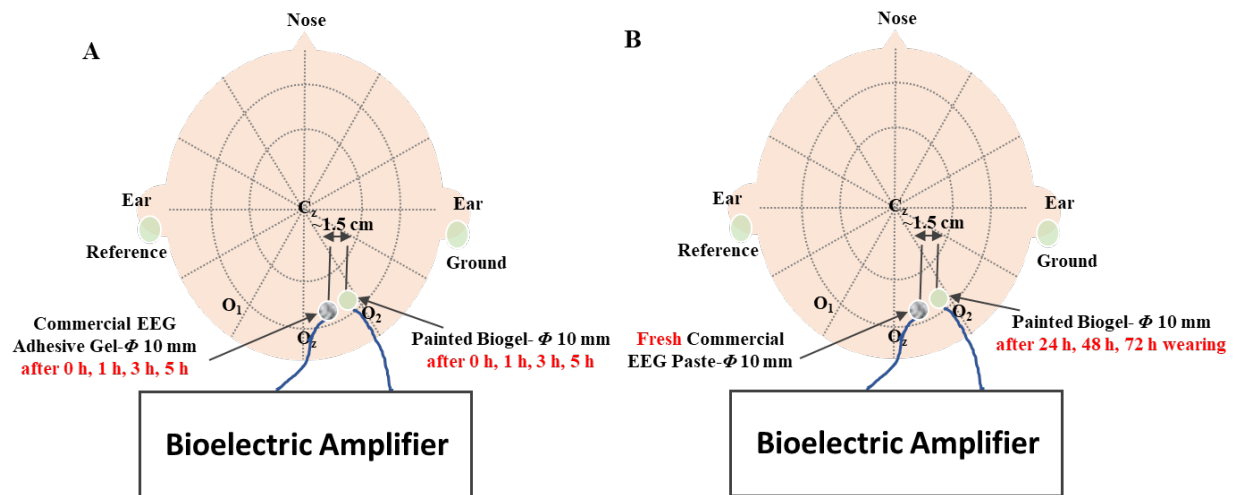
Fig. S22. **Schematic illustration of dual-channel EEG signal recording setup for long-term EEG recording.** EEG recording by the painted biogel electrode after continuous wearing for several hours (A) and for several days (B).
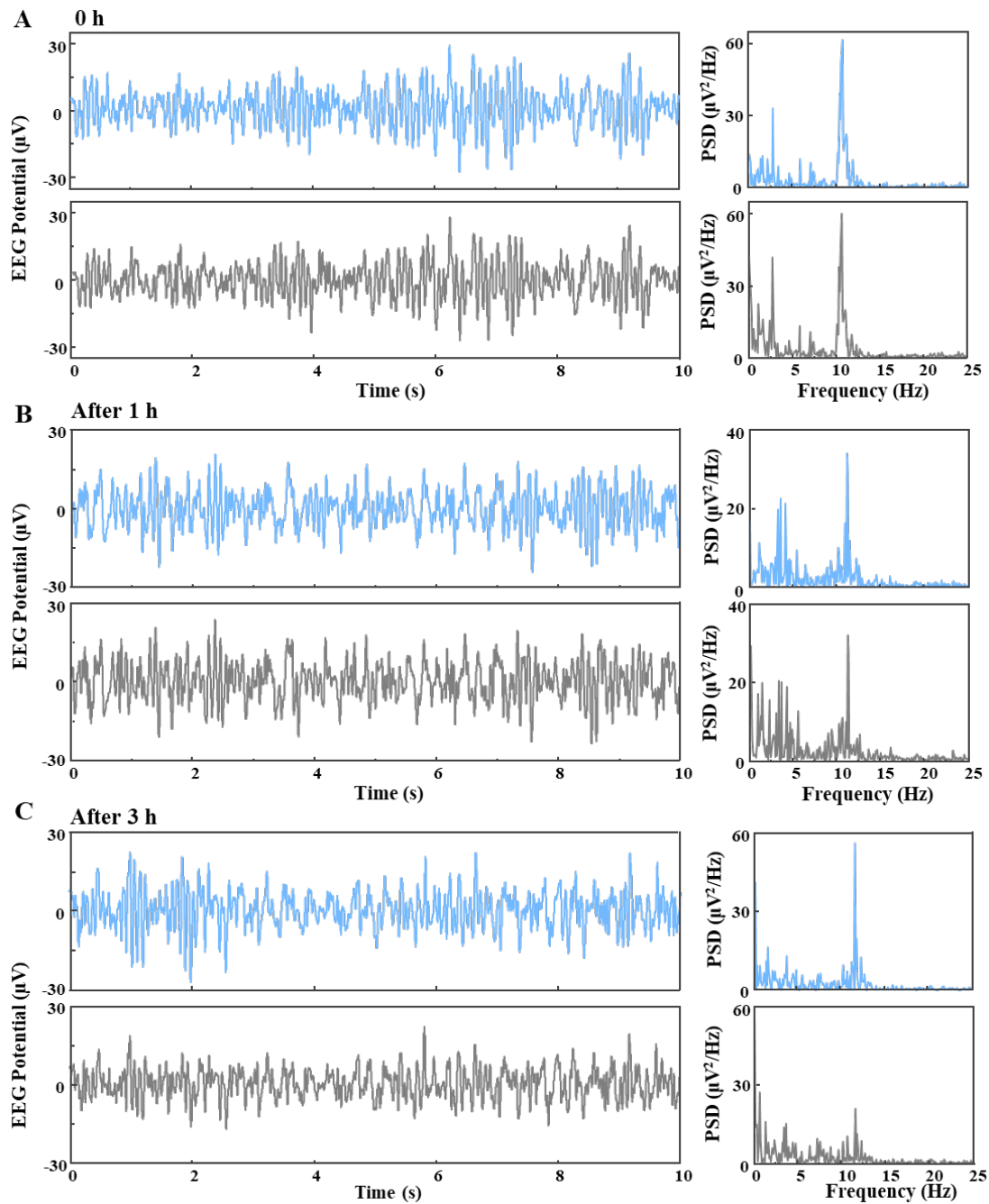
Fig. S23. EEG recording by the painted biogel electrode and commercial electrode after different duration. (A-C) EEG alpha rhythms recorded by the painted biogel electrode (upper, blue) and commercial EEG adhesive gel electrode (lower, grey) after continuous wearing for 0 h (A), 1 h (B), and 3 h (C) (left), and their corresponding PSD (right).

Fig. S24. EEG recording by the fresh commercial EEG paste electrodes which were placed for comparison with the biogel electrode after continuous wearing for different duration. (A-D) EEG alpha rhythms recorded by the fresh commercial EEG paste electrode for comparison with the biogel electrode after continuous wearing for 0 h (A), 24 h (B), 48h (C), and 72 h (D) (left), and their corresponding PSD (right).

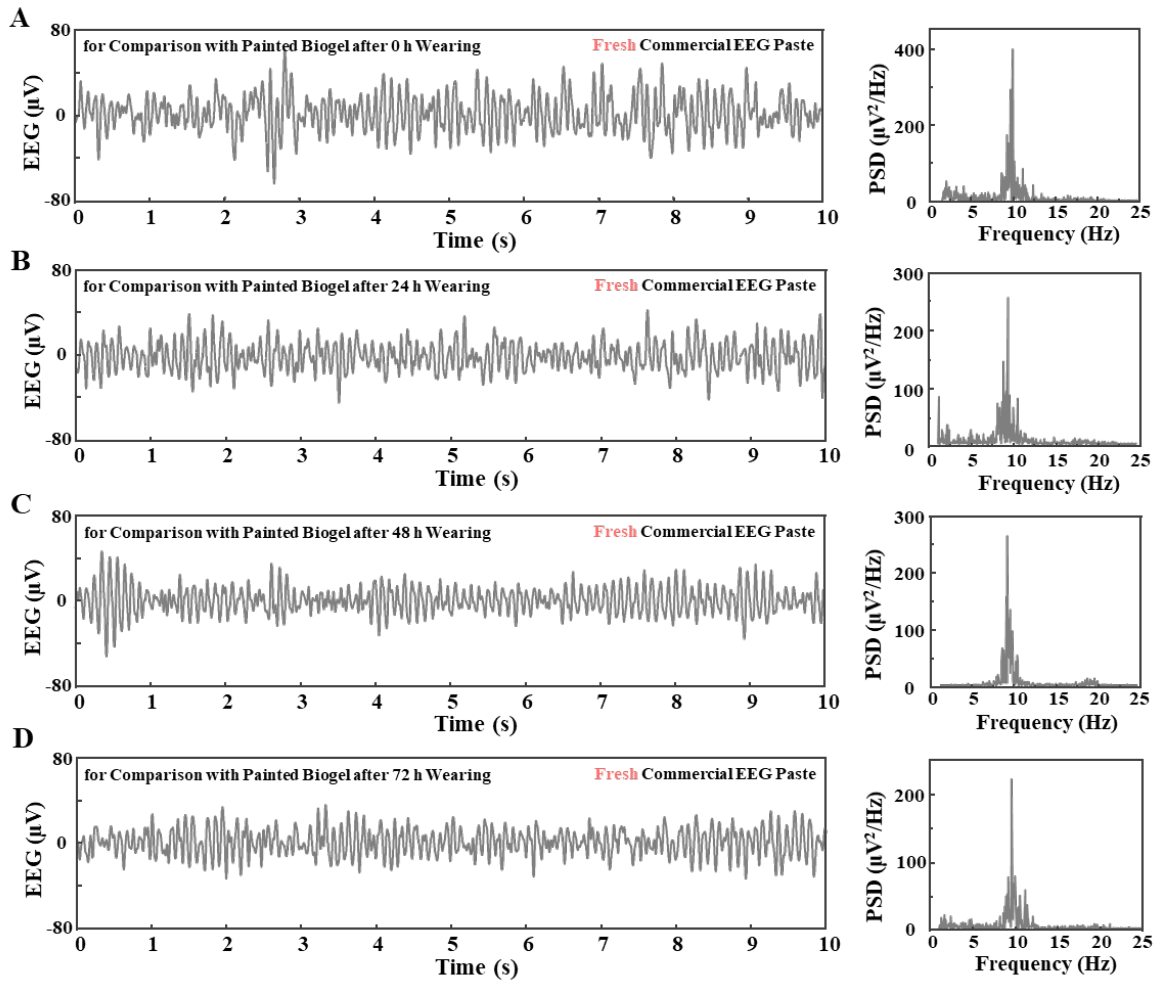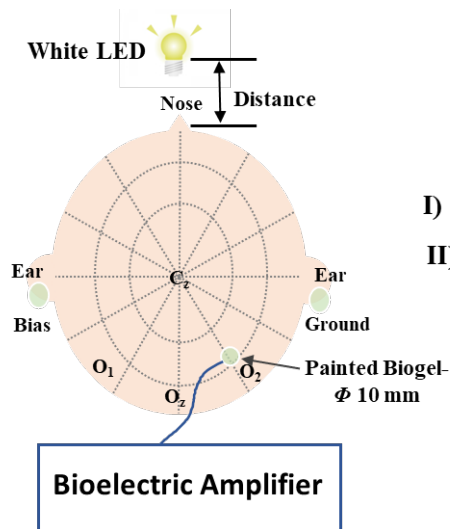**Fig. S25. Schematic illustration of the experimental setup for recording SSVEPs induced by the LED stimulation**. For eye-closed and eye-open situations, experiments were conducted in dark and bright room, respectively.

Based on the experimental setup for the SSVEP recording under LED stimulation (fig. S25), first, an LED flicker with the frequency of 10 Hz was placed in front of the subject at eye level in a dark and quiet room with the subject closing his eyes in a relaxed state to see if the EEG alpha rhythm would be synchronized or not. And the distance between the LED and the subject was adjusted to determine the optimized distance for further SSVEP experiments. Different distances indicate stimulation with different light intensities; in detail, the light stimulation intensities were ~3740 nW/cm^2 and ~118 nW/cm^2 for distances of ~5 cm and ~60 cm, respectively. When the LED flicker was placed too close to the eyes (~ 5 cm), the alpha rhythm was diminished with the attenuated amplitude and decreased characteristic peak intensity in the PSDA during the LED stimuli (fig. S26A and S26B); this may be attributed to the increased attention degree induced by the too intense light. The recorded alpha rhythm showed an augmented amplitude and increased PSDA peak intensity when the LED flicker was placed at an appropriate distance (~ 60 cm), indicating that the alpha rhythm was synchronized with the LED stimulation (fig. S26C and S26D).

Based on the above alpha rhythm synchronization results, further SSVEP recording by the painted biogel electrode was carried out, in which the subjects kept their eyes open during LED stimulation with the LED-eye distance of ~ 60 cm. 12-Hz LED flickering stimulus with different light intensities were initially conducted to observe the effect of the light intensity on the synchronization of the EEG. Compared to EEG signals recorded with no LED stimulation, EEG signals recorded under LED stimulus with different appropriate light intensities of ~32 nW/cm^2, ~ 53 nW/cm^2, and ~ 118 nW/cm^2, showed prominent peaks at 12 Hz in their PSDA with the peak amplitude increased with the increment of light intensity, indicating the heightened synchronization of the EEG signals with the light intensity augmentation (fig. S27). Then, a LED flicker with different frequencies of 4 Hz, 6 Hz, 8 Hz, 10 Hz, 14 Hz, 16 Hz, 18 Hz, 24 Hz, 28 Hz, 36 Hz, and 48 Hz was utilized to see if the EEG rhythm would be accordingly synchronized or not.
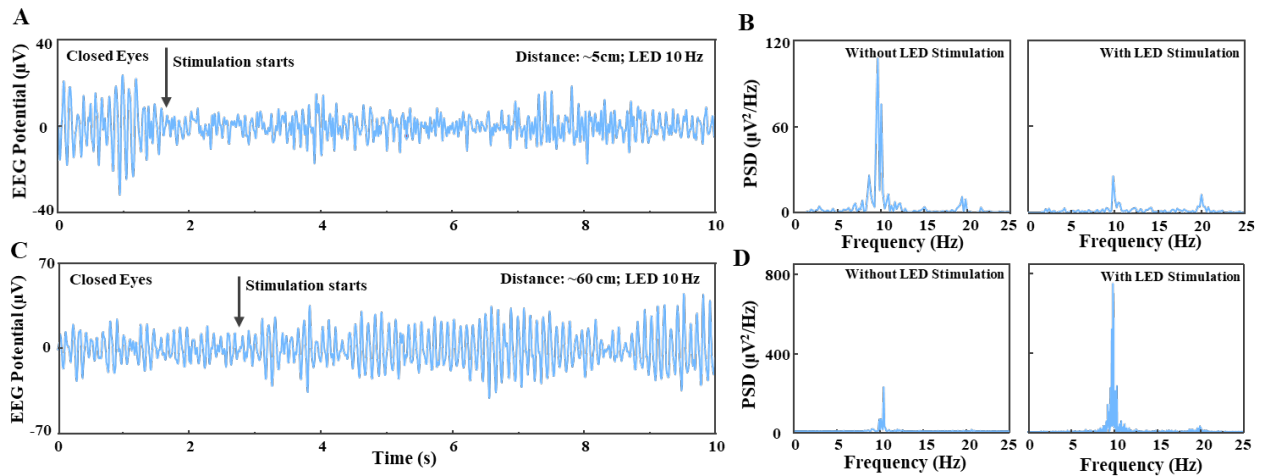
Fig. S26. EEG alpha rhythms recorded by the biogel electrode before and during LED stimulation with the frequency of 10 Hz. (A) EEG alpha rhythms recorded by the painted biogel electrode before and during LED stimulation with the frequency of 10 Hz and the LED-eye distance of ~ 5cm. (B) PSDA calculated from EEG signals in (A). (C) EEG alpha rhythms recorded before and during LED stimulation with the frequency of 10 Hz and the distance of ~ 60 cm. (D) PSDA calculated from EEG signals in (C).
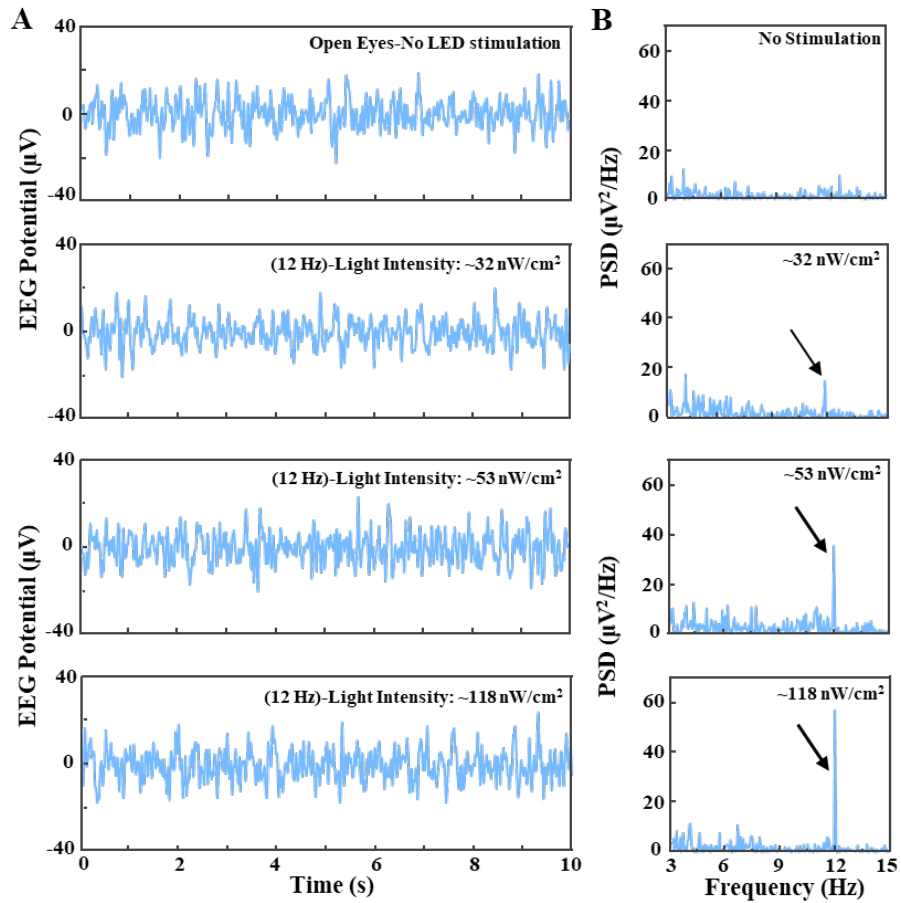
Fig. S27. EEG recording by the biogel electrode in the eye-open paradigm without LED stimulation and during LED stimulation with frequency of 12 Hz and different light intensity. (A) EEG signals recorded by the biogel electrode with light intensity of ~ 32 nW/cm^2, ~ 53 nW/cm^2, ~ 118 nW/cm^2. (B) PSDA calculated from EEG signals in (A).
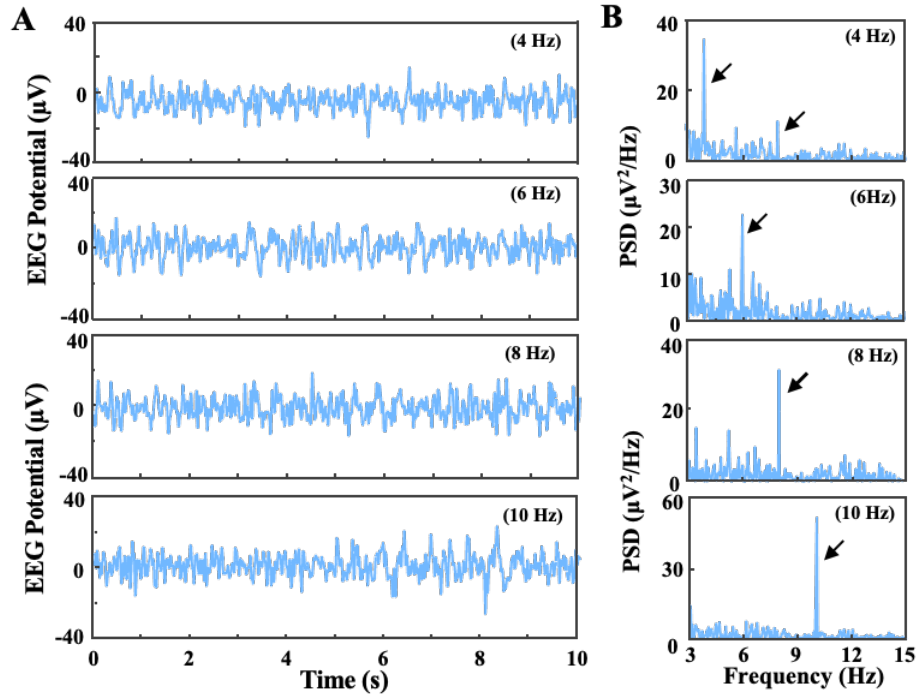
Fig. S28. SSVEPs recorded by the biogel electrode during LED stimulation. (A) SSVEPs recorded by the painted biogel electrode with the LED stimulation frequency of 4 Hz, 6 Hz, 8 Hz and 10 Hz. (B) PSDA calculated from EEG signals in (A).
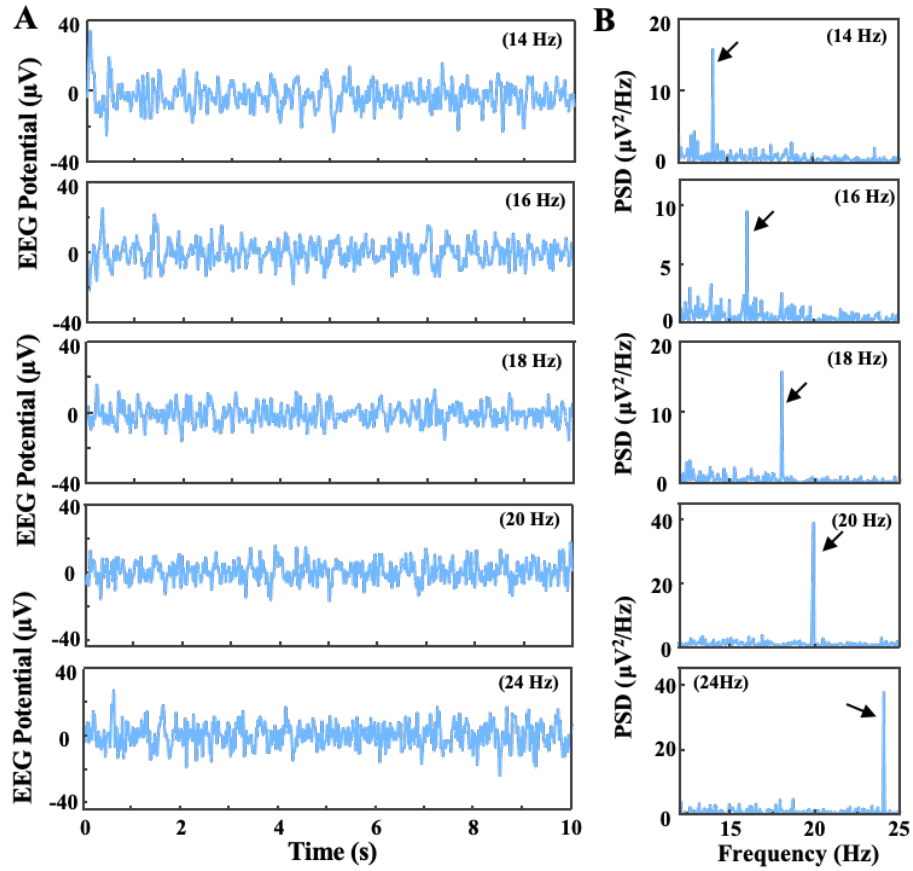
Fig. S29. SSVEPs recorded by the biogel electrode during LED stimulation. SVEPs recorded by the painted biogel electrode with the LED stimulation frequency of 14 Hz, 16 Hz, 18 Hz, 20 Hz and 24 Hz. (B) PSDA calculated from EEG signals in (A).
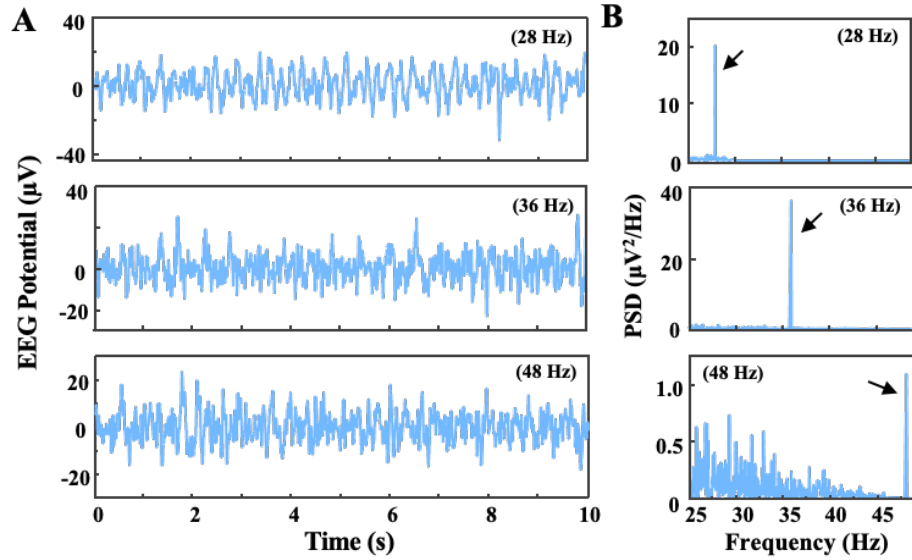
Fig. S30. SSVEPs recorded by the biogel electrode during LED stimulation. (A) SSVEPs recorded by the painted biogel electrode with the LED stimulation frequency of 28 Hz, 36 Hz and 48 Hz. (B) PSDA calculated from EEG signals in (A).
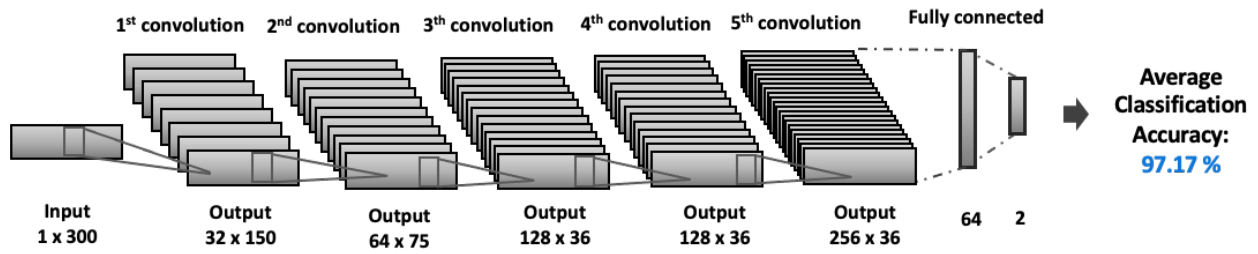
Fig. S31. Schematic illustration showing the seven-layer CNN model with five 1D convolutional layers followed by two fully connected layers. Here the time length of the input illustrated is 3 s and the average classification accuracy is 97.17% for all subjects.

Fig. S31 shows the detailed framework of the CNN model which contains five one-dimensional (1D) convolutional layers followed by two fully connected layers. This CNN model allows for the detection of hidden features that cannot be detected by simple filtering, and for the collection of the relevant activation from previous layers to be classified by the fully connected layer.
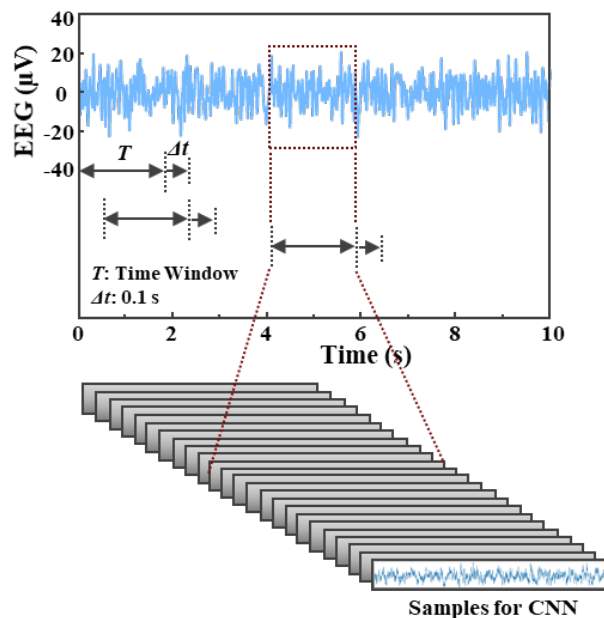
Fig. S32. Schematic illustration showing how to obtain samples from each SSVEP trial for the convolutional neural network model. T refers to the time window, and Δt means the time shift (0.1 s time shift was used).

Table S1. Biogel recipes with varying compositions.

	Gelatin (Type-A)	Sodium Chloride	Sodium Citrate	Citric Acid	Glycerol	Deionized Water
Biogel-Gly0/4	2g-175 Bloom	0.464 g	0 g	0 g	0 g	4 ml
Biogel-Gly1/4	2g-175 Bloom	0.464 g	0 g	0 g	1 g	4 ml
Biogel-Gly2/4	2g-175 Bloom	0.464 g	0 g	0 g	2 g	4 ml
Biogel-Gly3/4	2g-175 Bloom	0.464 g	0 g	0 g	3 g	4 ml
Biogel-Gly4/4	2g-175 Bloom	0.464 g	0 g	0 g	4 g	4 ml
Biogel-Gly6/4	2g-175 Bloom	0.464 g	0 g	0 g	6 g	4 ml
Biogel with 3.5 wt% NaCl	2g-175 Bloom	0.145 g	0 g	0 g	3 g	4 ml
Biogel with 2 M NaCl	2g-175 Bloom	0.464 g	0 g	0 g	3 g	4 ml
Biogel with 3 M NaCl	2g-175 Bloom	0.696 g	0 g	0 g	3 g	4 ml
Biogel-175 Bloom	2g-175 Bloom	0.464 g	0 g	0 g	3 g	4 ml
Biogel-300 Bloom	2g-300 Bloom	0.464 g	0 g	0 g	3 g	4 ml
Biogel-300 Bloom with Na$_3$Cit	2g-300 Bloom	0.464 g	0.5 g	0.05 g	3 g	4 ml

Table S2. Comparison between the on-skin paintable biogel and other electrodes for long-term EEG recording.

Electrodes		Skin Contact Impedance	Long-term recording period	Electrode location	Stretchability	Additional fixture to secure electrode onto the head	Ref.
Dry Electrodes	**Ultrathin kirigami conductor**	28.9 kΩ (forearm)	—	Clean skin (forehead)	Over 400%	No	(*15*)
	Ultrathin epidermal electrode	—	2 weeks	Clean skin (auricle)	>50%	No	(*11*)
	Claw-like Electrode with conductive elastomer legs	20 kΩ	—	Scalp with short hairs	Compressible	Yes	(*14*)
Semi-dry Electrodes	**Elastic sponge electrode filled with saline**	~10 kΩ	5 h	Hairy scalp	50% compression	Yes	(*13*)
	Porous cellulose membrane swollen by saline solution + Ag/AgCl electrode+ bulky solution reservoir	6.64 ± 0.95 kΩ	8 h	Hairy scalp	Flexible (cellulose membrane)	Yes	(*12*)
	Superporous hydrogel swollen by saline + Ag/AgCl electrode	23.4 ± 1.1 kΩ	6 h	Hairy scalp	Flexible (hydrogel)	Yes	(*5*)
Wet Electrodes	**Flexible columnar hydrogel electrode**	13.15 ± 3.72 kΩ	8 h	Hairy scalp	>350% (hydrogel)	Yes	(*17*)
	Commercial EEG pastes/gels +Ag/AgCl electrode	6.78 kΩ	5 h	Hairy scalp	—	Yes	This work
	On-skin paintable biogel electrode	6.95 ± 0.97 kΩ	72 h	Hairy scalp	~500% (biogel)	No	This work

Movie S1. (separate file)

Direct painting of the biogel on skin surface and the spontaneous in-situ gelatinization of the fluidic biogel into stretchable solid-like gel.

REFERENCES AND NOTES

1. G. Buzsáki, C. A. Anastassiou, C. Koch, The origin of extracellular fields and currents—EEG, ECoG, LFP and spikes. *Nat. Rev. Neurosci.* **13**, 407–420 (2012).

2. T. Someya, M. Amagai, Toward a new generation of smart skins. *Nat. Biotechnol.* **37**, 382–388 (2019).

3. C. Wang, K. Xia, H. Wang, X. Liang, Z. Yin, Y. Zhang, Advanced carbon for flexible and wearable electronics. *Adv. Mater.* **31**, 1801072 (2019).

4. D. Gao, K. Parida, P. S. Lee, Emerging soft conductors for bioelectronic interfaces. *Adv. Funct. Mater.* **30**, 1907184 (2020).

5. G. Li, S. Wang, M. Li, Y. Y. Duan, Towards real-life EEG applications: Novel superporous hydrogel-based semi-dry EEG electrodes enabling automatically 'charge–discharge' electrolyte. *J. Neural Eng.* **18**, 046016 (2021).

6. G.-L. Li, J.-T. Wu, Y.-H. Xia, Q.-G. He, H.-G. Jin, Review of semi-dry electrodes for EEG recording. *J. Neural Eng.* **17**, 051004 (2020).

7. N. A. Alba, R. J. Sclabassi, M. Sun, X. T. Cui, Novel hydrogel-based preparation-free EEG electrode. *IEEE Trans. Neural Syst. Rehabil. Eng.* **18**, 415–423 (2010).

8. P. Pedrosa, P. Fiedler, L. Schinaia, B. Vasconcelos, A. C. Martins, M. H. Amaral, S. Comani, J. Haueisen, C. Fonseca, Alginate-based hydrogels as an alternative to electrolytic gels for rapid EEG monitoring and easy cleaning procedures. *Sensor. Actuat. B Chem.* **247**, 273–283 (2017).

9. H. Yuk, B. Lu, X. Zhao, Hydrogel bioelectronics. *Chem. Soc. Rev.* **48**, 1642–1667 (2019).

10. Y.-J. Huang, C.-Y. Wu, A. M.-K. Wong, B.-S. Lin, Novel active comb-shaped dry electrode for EEG measurement in hairy site. *IEEE Trans. Biomed. Eng.* **62**, 256–263 (2014).

11. J. J. Norton, D. S. Lee, J. W. Lee, W. Lee, O. Kwon, P. Won, S.-Y. Jung, H. Cheng, J.-W. Jeong, A. Akce, S. Umunna, I. Na, Y. H. Kwon, X.-Q. Wang, Z. J. Liu, U. Paik, Y. Huang, T. Bretl, W.-H. Yeo, J. A. Rogers, Soft, curved electrode systems capable of integration on the auricle as a persistent brain–computer interface. *Proc. Natl. Acad. Sci. U.S.A.* **112**, 3920–3925 (2015).

12. J.-Y. Kim, Y. J. Yun, J. Jeong, C.-Y. Kim, K.-R. Müller, S.-W. Lee, Leaf-inspired homeostatic cellulose biosensors. *Sci. Adv.* **7**, eabe7432 (2021).

13. S. Lin, J. Liu, W. Li, D. Wang, Y. Huang, C. Jia, Z. Li, M. Murtaza, H. Wang, J. Song, Z. Liu, K. Huang, D. Zu, M. Lei, B. Hong, H. Wu, A flexible, robust, and gel-free electroencephalogram electrode for noninvasive brain-computer interfaces. *Nano Lett.* **19**, 6853–6861 (2019).

14. M. Mahmood, D. Mzurikwao, Y.-S. Kim, Y. Lee, S. Mishra, R. Herbert, A. Duarte, C. S. Ang, W.-H. Yeo, Fully portable and wireless universal brain–machine interfaces enabled by flexible scalp electronics and deep learning algorithm. *Nat. Mach. Intell.* **1**, 412–422 (2019).

15. P. Won, J. J. Park, T. Lee, I. Ha, S. Han, M. Choi, J. Lee, S. Hong, K.-J. Cho, S. H. Ko, Stretchable and transparent kirigami conductor of nanowire percolation network for electronic skin applications. *Nano Lett.* **19**, 6087–6096 (2019).

16. L. Tian, B. Zimmerman, A. Akhtar, K. J. Yu, M. Moore, J. Wu, R. J. Larsen, J. W. Lee, J. Li, Y. Liu, B. Metzger, S. Qu, X. Guo, K. E. Mathewson, J. A. Fan, J. Cornman, M. Fatina, Z. Xie, Y. Ma, J. Zhang, Y. Zhang, F. Dolcos, M. Fabiani, G. Gratton, T. Bretl, L. J. Hargrove, P. V. Braun, Y. Huang, J. A. Rogers, Large-area MRI-compatible epidermal electronic interfaces for prosthetic control and cognitive monitoring. *Nat. Biomed. Eng.* **3**, 194–205 (2019).

17. G. Shen, K. Gao, N. Zhao, Z. Yi, C. Jiang, B. Yang, J. Liu, A novel flexible hydrogel electrode with a strong moisturizing ability for long-term EEG recording. *J. Neural Eng.* **18**, 066047 (2021).

18. X. Sheng, Z. Qin, H. Xu, X. Shu, G. Gu, X. Zhu, Soft ionic-hydrogel electrodes for electroencephalography signal recording. *Sci. China Technol. Sci.* **64**, 273–282 (2021).

19. C. Wang, T. Yokota, T. Someya, Natural biopolymer-based biocompatible conductors for stretchable bioelectronics. *Chem. Rev.* **121**, 2109–2146 (2021).

20. M. Baumgartner, F. Hartmann, M. Drack, D. Preninger, D. Wirthl, R. Gerstmayr, L. Lehner, G. Mao, R. Pruckner, S. Demchyshyn, L. Reiter, M. Strobel, T. Stockinger, D. Schiller, S. Kimeswenger, F. Greibich, G. Buchberger, E. Bradt, S. Hild, S. Bauer, M. Kaltenbrunner, Resilient yet entirely degradable gelatin-based biogels for soft robots and electronics. *Nat. Mater.* **19**, 1102–1109 (2020).

21. Z. Qin, X. Sun, H. Zhang, Q. Yu, X. Wang, S. He, F. Yao, J. Li, A transparent, ultrastretchable and fully recyclable gelatin organohydrogel based electronic sensor with broad operating temperature. *J. Mater. Chem. A* **8**, 4447–4456 (2020).

22. L. Han, K. Liu, M. Wang, K. Wang, L. Fang, H. Chen, J. Zhou, X. Lu, Mussel-inspired adhesive and conductive hydrogel with long-lasting moisture and extreme temperature tolerance. *Adv. Funct. Mater.* **28**, 1704195 (2018).

23. C. Childs, Body temperature and clinical thermometry. *Handb. Clin. Neurol.* **157**, 467–482 (2018).

24. F. Suarez, A. Nozariasbmarz, D. Vashaee, M. C. Öztürk, Designing thermoelectric generators for self-powered wearable electronics. *Energ. Environ. Sci.* **9**, 2099–2113 (2016).

25. Y. Mosleh, W. de Zeeuw, M. Nijemeisland, J. C. Bijleveld, P. van Duin, J. A. Poulis, The structure–property correlations in dry gelatin adhesive films. *Adv. Eng. Mater.* **23**, 2000716 (2021).

26. S. Yang, Y. Zhang, T. Wang, W. Sun, Z. Tong, Ultrafast and programmable shape memory hydrogel of gelatin soaked in tannic acid solution. *ACS Appl. Mater. Interfaces* **12**, 46701–46709 (2020).

27. J.-H. Kim, S.-R. Kim, H.-J. Kil, Y.-C. Kim, J.-W. Park, Highly conformable, transparent electrodes for epidermal electronics. *Nano Lett.* **18**, 4531–4540 (2018).

28. L. Pan, P. Cai, L. Mei, Y. Cheng, Y. Zeng, M. Wang, T. Wang, Y. Jiang, B. Ji, D. Li, X. Chen, A compliant ionic adhesive electrode with ultralow bioelectronic impedance. *Adv. Mater.* **32**, 2003723 (2020).

29. L. Kalevo, T. Miettinen, A. Leino, S. Kainulainen, H. Korkalainen, K. Myllymaa, J. Töyräs, T. Leppänen, T. Laitinen, S. Myllymaa, Effect of sweating on electrode-skin contact impedances and artifacts in EEG recordings with various screen-printed Ag/Agcl electrodes. *IEEE Access* **8**, 50934–50943 (2020).

30. H. Y. Y. Nyein, M. Bariya, B. Tran, C. H. Ahn, B. J. Brown, W. Ji, N. Davis, A. Javey, A wearable patch for continuous analysis of thermoregulatory sweat at rest. *Nat. Commun.* **12**, 1823 (2021).

31. F. Ershad, A. Thukral, J. Yue, P. Comeaux, Y. Lu, H. Shim, K. Sim, N.-I. Kim, Z. Rao, R. Guevara, L. Contreras, F. Pan, Y. Zhang, Y.-S. Guan, P. Yang, X. Wang, P. Wang, X. Wu, C. Yu, Ultra-conformal drawn-on-skin electronics for multifunctional motion artifact-free sensing and point-of-care treatment. *Nat. Commun.* **11**, 3823 (2020).

32. L. Zhang, K. S. Kumar, H. He, C. J. Cai, X. He, H. Gao, S. Yue, C. Li, R. C.-S. Seet, H. Ren, J. Ouyang, Fully organic compliant dry electrodes self-adhesive to skin for long-term motion-robust epidermal biopotential monitoring. *Nat. Commun.* **11**, 4683 (2020).

33. A. J. Casson, D. C. Yates, S. J. Smith, J. S. Duncan, E. Rodriguez-Villegas, Wearable electroencephalography. *IEEE Eng. Med. Biol. Mag.* **29**, 44–56 (2010).

34. C. Babiloni, C. Del Percio, L. Arendt-Nielsen, A. Soricelli, G. L. Romani, P. M. Rossini, P. Capotosto, Cortical EEG alpha rhythms reflect task-specific somatosensory and motor interactions in humans. *Clin. Neurophysiol.* **125**, 1936–1945 (2014).

35. A. K. Robinson, P. Venkatesh, M. J. Boring, M. J. Tarr, P. Grover, M. Behrmann, Very high density EEG elucidates spatiotemporal aspects of early visual processing. *Sci. Rep.* **7**, 16248 (2017).

36. S. M. Lee, J. H. Kim, H. J. Byeon, Y. Y. Choi, K. S. Park, S.-H. Lee, A capacitive, biocompatible and adhesive electrode for long-term and cap-free monitoring of EEG signals. *J. Neural Eng.* **10**, 036006 (2013).

37. C. S. Herrmann, Human EEG responses to 1–100 Hz flicker: Resonance phenomena in visual cortex and their potential correlation to cognitive phenomena. *Exp. Brain Res.* **137**, 346–353 (2001).

38. S. Park, S. W. Heo, W. Lee, D. Inoue, Z. Jiang, K. Yu, H. Jinno, D. Hashizume, M. Sekino, T. Yokota, K. Fukuda, K. Tajima, T. Someya, Self-powered ultra-flexible electronics via nano-grating-patterned organic photovoltaics. *Nature* **561**, 516–521 (2018).

39. Y. Bai, B. Chen, F. Xiang, J. Zhou, H. Wang, Z. Suo, Transparent hydrogel with enhanced water retention capacity by introducing highly hydratable salt. *Appl. Phys. Lett.* **105**, 151903 (2014).

40. J. F. Martucci, R. A. Ruseckaite, Biodegradation behavior of three-layer sheets based on gelatin and poly (lactic acid) buried under indoor soil conditions. *Polym. Degrad. Stab.* **116**, 36–44 (2015).

41. J. Baier Leach, K. A. Bivens, C. W. Patrick Jr, C. E. Schmidt, Photocrosslinked hyaluronic acid hydrogels: Natural, biodegradable tissue engineering scaffolds. *Biotechnol. Bioeng.* **82**, 578–589 (2003).